Nanoscale

Accepted Manuscript

This article can be cited before page numbers have been issued, to do this please use: E. Pargoletti, U. H. Hossain, I. Di Bernardo, H. Chen, T. P. Tran, J. Lipton-Duffin, G. Cappelletti and A. Tricoli, *Nanoscale*, 2019, DOI: 10.1039/C9NR08901B.

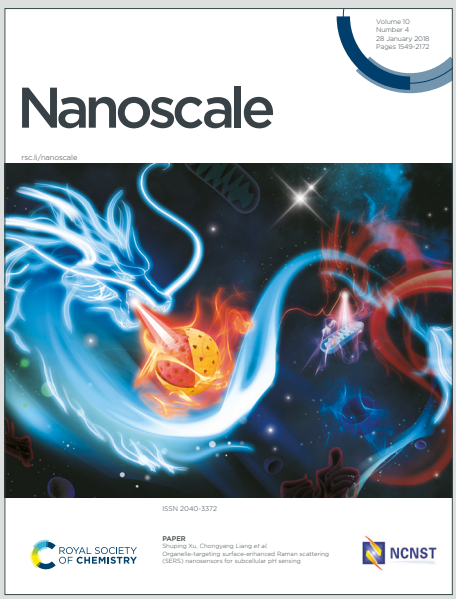

ROYAL SOCIETY OF CHEMISTRY

rsc.li/nanoscale

Room-Temperature Photodetectors and VOCs sensors based on Graphene Oxide – ZnO Nano-Heterojunctions

View Article Online
DOI: 10.1039/C9NR08901B

Eleonora Pargoletti,[1,2] Umme H. Hossain,[3] Iolanda Di Bernardo,[4] Hongjun Chen,[4] Thanh Tran-Phu,[4] Josh Lipton-Duffin,[5] Giuseppe Cappelletti,[1,2*] and Antonio Tricoli[4*]

[1] *Dipartimento di Chimica, Università degli Studi di Milano, via Golgi 19, 20133, Milano, Italy*
[2] *Consorzio Interuniversitario Nazionale per la Scienza e Tecnologia dei Materiali (INSTM), Via Giusti 9, 50121, Firenze, Italy*
[3] *Department of Electronic Materials Engineering, Research School of Physics and Engineering, The Australian National University, Canberra ACT 2601, Australia*
[4] *Nanotechnology Research Laboratory, College of Engineering and Computer Science, The Australian National University, Canberra ACT 2601, Australia*
[5] *Institute for Future Environments (IFE), Central Analytical Research Facility (CARF), Queensland University of Technology (QUT), Brisbane, Australia*

e-mails: giuseppe.cappelletti@unimi.it; antonio.tricoli@anu.edu.au

Abstract

The rapid development of smart wearable electronics is driving the engineering of novel miniaturized sensing materials that can rapidly respond to very small changes in the concentration of biomarkers at room temperature. Carbon-based nanomaterials offer numerous attractive properties such as low resistivity, good mechanical robustness and integration potential, but lack a strong detection and transduction mechanism for the measurement of chemical molecules or photons. Here, we present a three-dimensional nanostructured architecture comprising of optimally integrated graphene oxide (GO) – ZnO heterojunctions for the room temperature sensing of volatile biomarkers. We show that this layout also provides excellent response to UV light showcasing its applicability as visible-blind photodetector. Notably, the optimal integration of well-dispersed GO nanodomains in a 3D ZnO network significantly enhances the room-temperature chemical sensitivity and light responsivity, while higher GO contents drastically worsen the material performance. This is attributed to the different roles of GO at low and high contents. Small amounts of GO lead to the formation of electron depleted nano-heterojunctions with excellent electron-hole separation efficiency. In contrast, large GO amounts form a percolating electrical network short-cutting the light and chemical-sensing ZnO nanoparticles. Our optimal GO-ZnO demonstrates 33 $A \cdot W^{-1}$ responsivity to UV light as well as the room temperature detection of down to 100 ppb of volatile organic compounds. We believe that these findings provide guidelines for the future engineering of hybrid carbon-metal oxide devices for application extending from optoelectronics to chemical sensing and electrocatalysis.

Keywords

Nano-heterojunctions; graphene oxide; zinc oxide; visible-blind photo-detectors; room temperature chemical sensing

Introduction

The latest achievements in wearable and portable electronic is driving the demand for miniaturized sensor materials capable of detecting a wide variety of signals ranging from UV light exposure to biomarkers[1–3]. The challenges and potential of these few-millimetres in size devices are: (*i*) the implementation in on-chip electronic systems with ultra-low power consumption; (*ii*) the replacement of the traditional expensive and time-consuming analytical instrumentations; (*iii*) the engineering of next-generation wireless sensors[4].

Monitoring of gaseous components in real matrices is of particular practical importance with applications extending from environmental protection[5,6], medical diagnostics[4,7], industrial manufacturing[8,9], agriculture (*e.g.* biohazards, fruit ripening)[9], and safety (*e.g.* explosive detection). Recent success in non-invasive medical diagnostics based on human breath analysis, is pushing forward the development of extremely sensitive chemical sensors for ppb detection of specific analytes in a complex gas mixture, operating at room temperature[10]. Acetone, for example, is related to type 1 diabetes[11] since its concentration increases from a value in the range 300-900 ppb in healthy people to more than 1800 ppb in diabetics' breath. The detection of ethanol (< 100 ppm), on the other hand, can be useful for food quality monitoring in fermentation industries and medical applications[12]. Similarly, ethylbenzene, already widely studied for environmental pollution as a BTEX compound, has been recently recognized as one of the potential biomarkers for lung cancer detection (0.04 ppb in healthy humans *vs* 0.11 ppb in ill patients)[13–15].

Miniaturized chemoresistive gas nanodetectors, made of nanostructured metal oxides, can be a promising alternative to the traditional and more sophisticated analytical techniques (such as PTR-MS or gas chromatography)[16]. Nevertheless, they have poor selectivity, scarce life-time and they usually operate at high temperatures[3]. Among the most performing metal oxides, ZnO nanoparticles have been successfully used to sense some VOCs, as ethanol and acetone, down to part-per-billion level[5,17,18]. However, these devices have usually the disadvantage of high operating temperature, which in turn adversely affects their long-term stability. Nevertheless, the latter drawbacks can be moderated, for example, by co-synthesizing metal oxides with other oxides/non-metal elements[19,20] or by doping them with metal nanoparticles (such as Pt or Ag)[21]. Besides, another method recently explored is the coupling of the metal oxides with graphene-based materials[1,22]. Indeed, graphene possesses several optimal properties such as thermo-electric conduction and mechanical strength[13]. In this context, reduced graphene oxide (rGO) has been widely investigated and offers great potentialities for the gas sensing. On the contrary, pure graphene oxide (GO) has not been so studied due to its less defective structure and to the many functional groups on its surface if compared to rGO[23–25]. Nevertheless, GO has been reported to possess excellent electrical and mechanical properties[13] and its p-type semiconductor character[26–28] can be exploited to form a p-n heterojunction with various n-type gas sensing semiconductor. Hence, it is challenging to proper combine metal oxide semiconductors and GO; this is the main reason why we have decided to go ahead with our work. Moreover, GO functionalities can be the anchor points for the controlled chemical growth of metal oxide nanoparticles, thus giving rise to well-integrated composite materials. Moreover, there is still a lack of literature concerning on this topic. Specifically, the available literature[2,29,30] reports data about mechanically mixed or impregnated ZnO-GO compounds. For instance, Vessalli *et al.*[29] described ZnO nanorods, with controlled size and morphology, grown through a wet deposition on gold interdigitated electrodes, previously covered with graphene oxide, through the same synthetic route. Besides, Wang *et al.*[30] reported ZnO/GO nanocomposites by impregnation of GO with zinc oxide nanosheets.

Therefore, herein, nanostructured detectors based on an intimate incorporation of p-type GO nanodomains in an n-type 3D ZnO nano-architecture are reported. The properties of these ultraporous nano-heterojunction networks were characterized by a set of physical and chemical approaches providing insights on the role of GO in enhancing or inhibiting the photodetectivity and chemical-sensing mechanism of the networks. These nanocomposite materials were used to sense some representative VOCs such as ethanol (EtOH), acetone and ethylbenzene (EtBz) gas molecules, down to room temperature by exploiting UV light activation of the sensing reactions. We observed that small amount of GO leads to the formation of electron depleted nano-heterojunctions with excellent electron-hole separation efficiency. The latter were able to detect ppb VOCs concentrations (100 ppb) at room temperature. We also show that this optimal nanocomposite structure provides excellent response to UV light showcasing its applicability as visible-blind UV photodetector.

Experimental section

Synthesis of graphene oxide powder

Graphene Oxide (GO) was prepared by adopting a modified Hummers' method[31,32]. Concentrated H_2SO_4 (50 mL) was added to a mixture of graphite (1 g, Sigma-Aldrich, particle size < 20 μm) and $NaNO_3$ (1 g, Sigma-Aldrich), and the suspension was cooled down to 0 °C in an ice bath. $KMnO_4$ (6 g, Sigma-Aldrich, 98%) was slowly added to keep the reaction temperature below 10 °C. The solution was stirred for 4 h. Then, 100 mL of MilliQ water was introduced dropwise, keeping the suspension in the ice bath due to the highly exothermic reaction. The mixture was stirred for other 2 h at 70 – 80 °C and, finally, 200 mL of MilliQ water (at 60 °C) followed by 20 mL of 15 %wt H_2O_2 (from

View Article Online
DOI: 10.1039/C9NR08901B

dilution of 30 %wt H_2O_2 by Sigma-Aldrich) were slowly added. The brownish slurry was left to decant overnight at room temperature. Then, it was centrifuged several times at 8000 rpm. The remaining solid material was finally washed through a dialysis method by using Spectra/Pore® molecular porous membrane tubing, until the pH became neutral. Further, the precipitate was dried in oven at 60 °C.

Synthesis of pure and hybrid ZnO-GO materials

The appropriate amount of $Zn(NO_3)_2$ was dissolved in 3.0 mg mL^{-1} of GO suspension to have starting salt precursor-to-GO weight ratios from 4:1 to 32:1. The mixture was stirred (at 300 rpm) for 15 min at 50 °C and then 60 mL of an aqueous solution of ammonium hydroxide (25% v/v, 2.76 g) was slowly added. After the addition, the pH passed from 3 to 10 and the mixture was continuously stirred for other 5 h. The resultant product was centrifuged (at 8000 rpm) several times with MilliQ water, until the pH became neutral. Finally, it was dried in oven at 60 °C. A final calcination step under oxygen flux (6 h, 9 NL h^{-1}) followed to form a whitish precipitate.

Concerning the pure ZnO material, the same synthetic route was adopted without the initial addition of the GO suspension.

Deposition of pure and hybrid ZnO-GO materials on Interdigitated Electrodes

Powders were deposited on glass substrates topped with interdigitated Pt electrodes (IDEs) by hot-spray method. The IDEs were made of glass on which interdigitated Pt lines with 5 μm in width and space have been deposited (G-IDEAU5, DropSens, Oviedo, Spain)[33]. To remove any contamination from the electrodes, all substrates were sintered at 300 °C for 12 h and washed by several washing (ethanol)/drying cycles before deposition. Then, 4.0 mL of 2.5 mg mL^{-1} ethanol powders suspensions were sprayed by keeping constant the air-brush pressure (0.8 bar), the temperature of the heating plate (230 °C) and the deposition height (8 cm). A final calcination step at 350 °C for 1 h was performed to guarantee a good powders film adhesion on IDEs.

Physico-chemical characterizations

The BET surface area was determined by a multipoint BET method using the adsorption data in the relative pressure (p/p_0) range of 0.05–0.20 (Coulter SA3100 apparatus). Desorption isotherms were used to determine the total pore volume using the Barrett-Joyner-Halenda (BJH) method.

X-ray Diffraction (XRD) analyses were performed on a Philips PW 3710 Bragg-Brentano goniometer equipped with a scintillation counter, 1° divergence slit, 0.2 mm receiving slit and 0.04° soller slit systems. We employed graphite-monochromated Cu Kα radiation (Cu $K\alpha_1$ λ = 1.54056 Å, $K\alpha_2$ λ = 1.54433 Å) at 40 kV × 40 mA nominal X-rays power. Diffraction patterns were collected between 10° and 80° with a step size of 0.02° and a total counting time of about 1 h. A microcrystalline Si-powdered sample was used as a reference to correct for instrumental line broadening effects.

ATR-FTIR analyses were recorded by Nicolet 380 Spectrophotometer-Thermo Electron Corporation, between 4000 – 400 cm^{-1}.

Raman spectra were taken on a Renishaw InVia micro-Raman Spectrometer. A 50 mW, 532 nm diode laser was used for excitation. The spectrometer was equipped with a Nikon 50× objective lens (WD = 17 mm, NA = 0.45), which produced a focal spot of 1 μm^2 and a total power of 0.71 mW from the objective. All spectra were processed to remove cosmic rays using the inbuilt software package Wire 4.2. Raman spectra of graphite and graphene oxide samples have been deconvoluted in eight and five modes, respectively, by using the Lorentzian function and the intensity ratios between D and G bands have been calculated according to Atchudan *et al.*[34].

To evaluate powders optical band gaps by Kubelka-Munk elaboration, Diffuse Reflectance Spectra (DRS) were measured on a UV/Vis spectrophotometer Shimadzu UV-2600 equipped with an integrating sphere; a "total white" $BaSO_4$ was used as reference. In parallel, an estimation was also determined by Tauc plot elaboration (using λ of 370 nm) acquiring absorbance spectra in the range 300-800 nm through Agilent Cary 60 UV/Vis spectrophotometer. The porosity of ZnO nanoparticle networks of the films was estimated from the optical density and SEM visible thickness as suggested by Bo *et al.*[33], by adopting an absorption coefficient of 2.24×10^7 m^{-1} (at 370 nm for all the powders).

The morphology was investigated by using a Zeiss Ultraplus (filed-emission scanning electron microscopy, FESEM) at 3 kV coupled with an Energy Dispersive X-ray spectrophotometer (EDX) for the elemental analysis. Transmission Electron Microscope (TEM) analyses were performed on Hitachi H7100FA at 100 kV. The TEM grids

were prepared dropping the dispersed suspension of nanoparticles in ethanol onto a holey-carbon supported copper grid and drying it in air at room temperature overnight.

Thermogravimetric analyses were carried out by means of Metter Toledo Star and System TGA/DSC 3+ under air atmosphere (5 °C min^{-1} from 30 to 800°C).

View Article Online
DOI: 10.1039/C9NR08901B

X-ray Photoemission Spectroscopy (XPS) data were collected in a Thermofisher Kratos Axis Supra photoelectron spectrometer at the Central Analytical Research Facility of the Queensland University of Technology (Brisbane, Australia). The apparatus is equipped with a monochromated Al k_α source (1486.7 eV), and the spectra were calibrated with respect to their Fermi level. Survey spectra were acquired at pass energy 160, high resolution spectra at pass energy 20.

Cyclic Voltammetry (CV) analyses were carried out on Glassy Carbon (GC) working electrode, modified by drop casting (20 μL) of 0.5 mg mL^{-1} dimethylformamide powders (*i.e.* pure GO, ZnO, 32:1 ZnO/GO and ZnO mechanically mixed to GO with a corresponding ratio of about 32-to-1) suspensions. The electrochemical measurements were performed in a conventional three-electrode cell using a platinum foil as the counter electrode and a Saturated Calomel Electrode (SCE) as the reference one (E= 0.244 V vs SHE). A phosphate buffered saline solution (PBS) 0.1 M, at fixed pH 7.4, was utilized as the supporting electrolyte. Tests have been performed by adding $[Ru(NH_3)_6]Cl_3$ probe to have a final concentration in PBS equal to 3 mM. The CVs were recorded at room temperature by using an Autolab PGStat30 (Ecochemie, The Netherlands) potentiostat/galvanostat controlled by NOVA 2.0 software for data acquisition. A step potential of 0.005 V and a scan rate of 0.1 V s^{-1} were adopted.

Electrochemical Impedance Spectroscopy (EIS) experiments were carried out at -0.15 V (*i.e.* the potential at which the $[Ru(NH_3)_6]Cl_3$ probe is oxidized), with a range of frequencies between 65,000 and 0.1 Hz and an amplitude of 10 mV, using an Autolab PGSTAT30 (Ecochemie, The Netherlands) potentiostat/galvanostat equipped with an FRA module and controlled by GPES and FRA softwares. Impedance data were then processed with Z-View 3.1 software.

Gas sensing measurements and photodetector tests

For gas sensing of ethanol, acetone and ethylbenzene, O_2 (BOC Ltd) and N_2 (BOC Ltd) were controlled by mass flow controller (Bronkhorst), with a total gas flow rate of 0.5 L min^{-1}. The target gases (10 ppm in N_2, Coregas) were diluted to 1 ppm and lower concentrations by using the simulated air (0.1 L min^{-1} O_2 + 0.4 L min^{-1} N_2, BOC Ltd) before purging into the chamber, keeping constant the total flow rate of 0.5 L min^{-1}. The temperature of the hotplate in the gas sensing chamber (Linkam) was controlled by a temperature controller and, when UV light was exploited, the samples were illuminated through a quartz window by a solar simulator (NewSpec, LCS-100) with an FGUV5-UV – Ø25 mm UG5 Colored Glass Filter (AR Coated: 290 - 370 nm, Thorlabs Inc). Indeed, the operating temperature was varied between 25 and 350 °C (exploiting the UV irradiations for T lower than 350 °C). For the gas sensing measurements, two gold probes were separately placed on top of the powders covered IDEs, and the dynamic response was recorded by an electrochemical workstation (CHI 660E, USA) by applying a bias of 1.0 V. The sensor response is reported as: $(R_{air} / R_{analyte}) - 1$, where R_{air} is the film resistance in air and $R_{analyte}$ is the film resistance at a given concentration of the target gas[11]. The sensor response time is the time needed to reach the 90% of the sensor response, while the recovery time is the time necessary to recover the 90% of the response[35].

As concern the powders photodetector properties, photo- and dark-currents were measured at 25 °C with an LCS-100 Series Small Area Solar Simulator (Newport Co.). The electrode active surface was equal to 0.4 cm^{-2} and the irradiation power at 370 nm was 19.2 μW·cm^{-2}. The responsivity and detectivity were, then, calculated according to the equations reported elsewhere[33].

Results and Discussion

ZnO-GO Nano-heterojunction Synthesis

A comprehensive range of ZnO-GO nanocomposite structures were synthesized varying the ZnO/GO ratio from 4 to 32 (specifically, 4:1, 8:1, 16:1 and 32:1). The XRD, FTIR and Raman analyses (Fig. 1a – c and Fig. S1a, b; green spectra) confirm the effective graphite oxidation and its exfoliation, which is highlighted by the characteristic peaks/bands of graphene oxide[23,32,36–38]. The X-ray diffraction patterns (Fig. 1a) shows the appearance of the (0 0 1) GO plane peak at a 2θ of 12°,[32] and the simultaneous decreasing contribution from the (0 0 2) graphite plane. Infrared spectroscopy also reveals the bands at 1043, 1616 and 1716 cm^{-1} related to the stretching modes of C-O-C, C=C and

View Article Online
DOI: 10.1039/C9NR08901B

C=O bonds, respectively[32]. Furthermore, by deconvoluting the Raman spectra of both the precursor graphite and the as-prepared graphene oxide (Fig. S1c and d), the successful oxidation is further corroborated by the shifting of the D and G bands with respect to the pure graphite as well as their intensity ratio (I_D/I_G). The D band is connected to a disordered structure, originated by structural defects, edge effects and dangling sp^2 carbon bonds that break the symmetry, while the G peak results from the first order scattering of E_{2g} mode of the sp^2 carbon domains[39]. Both bands position and intensity depend on several factors, such as the doping level, the number of layers and the presence of structural defects.[40]. Here, in the pristine graphite the D and G peaks positions are centered at 1347 and 1576 cm^{-1}, while for GO they appear at 1310 and 1564 cm^{-1}, respectively (Fig. 1c and S1c, d). Moreover, the GO I_D/I_G ratio is ~1 (*i.e.* about four times the one of graphite), a value typically reported for this compound since, during the oxidation process, oxygen functional groups were introduced into the graphitic chain causing a rise in the D band intensity[41]. The achievement of graphene oxide multi-stacked sheets is also confirmed by TEM analysis (Figure 1d). The surface area and the total pores volume (Table 1, 2nd and 3rd columns) show a slight increase from 11 *vs* 30 $m^2\ g^{-1}$ and a decrease from 0.030 *vs* 0.010 $cm^3\ g^{-1}$, respectively. The latter is a probable consequence of the very exothermic reaction leading to a collapse of the void space.

Zinc oxide nanoparticles were grown on the GO surface by exploiting its abundant oxidized groups. A similar set of structural analyses evidenced the actual presence and progressive growth of the ZnO nanodomains by increasing the Zn salt precursor concentration to GO weight ratio from 4 to 32. Specifically, the XRD spectra (Fig. 1a and S1a) show the main zinc oxide polymorphic phase, *i.e.* wurtzite[42,43], for both the hybrid compounds with the ZnO crystal size increasing from 11 to 22 and 44 nm with increasing ZnO/GO ratio from 0 to 4:1 and 32:1, thus approaching the value for pure ZnO of 77 nm (Table 1, 4th column). The FTIR and Raman analyses further confirm this trend (Fig. 1bc and S1b). The FTIR stretching mode of the Zn-O-Zn bonds (at ~500 cm^{-1}) appear in all the zinc oxide-containing samples. The Raman spectra of both pure ZnO and hybrid compounds show A_1 LO (at 594 cm^{-1}) and E_2 high (at 454 cm^{-1}) bands relative to ZnO particles[34]. Notably, in the case of the 4:1 ZnO/GO ratio, all the structural analyses reveal the presence of a small quantity of the graphene oxide sheets underneath the ZnO nanoparticles (Fig. 1a – c, red line). In contrast, this is not visible in the 32:1 sample. The specific surface areas of the ZnO-GO composite materials are higher (25 and 11 $m^2\ g^{-1}$) than that (9 $m^2\ g^{-1}$) of the pure ZnO[44], following a decreasing trend with the increase of ZnO content (Table 1, 2nd column). The same trend is observed for the total pores volume data (Table 1, 3rd column).

The growth of the ZnO nanoparticles is also confirmed by the TEM and EDX analyses. In particular, the 4:1 ZnO/GO ratio shows packed agglomerates with dimensions of around 20 nm (Fig. 1e), which are smaller than the 32:1 ratio ones, having a size of ~50-60 nm (Fig. 1f). Moreover, both EDX spectra (Fig. 1g and h) effectively confirm the presence of zinc species for all the composite materials concentrations. Figures 2a – c show a significant change in the material morphology switching from a pure ZnO to a 32:1 and 4:1 ZnO/GO composition. The pure ZnO displays agglomerates made of spherical particles with diameters of ~100 nm (Fig. 2a). The 4:1 sample analysis reveals the presence of flakes (Fig. 2b), probably arising by the GO presence, that are not completely covered by the metal oxide. Increasing the ZnO content, particles tend to agglomerate forming nanorods with diameters of around 80-100 nm and length of up to several hundreds of nanometers (Fig. 2c). This nanorod-surface texture, which has not been observed for the other ZnO/GO hybrid material and for the pure ZnO, may be attributed to a preferential growth of zinc oxide along the (1 0 1) plane, as emphasized by the strong XRD diffraction peak in this direction. The small GO amount present may help inhibiting growth in the other planes.

Thermogravimetric analyses reveal a very high stability of either pure ZnO[45] or hybrid ZnO-GO samples (Fig. 3a). Notably, even at temperatures of up to 800 °C a mass loss of only ~2.5% is measured. In contrast, the pure GO (Fig. 3a, green line) decomposes in several stages. First a weight loss due to moisture and interstitial water occurs between 60 and 110 °C. The thermal stability of adsorbed water is influenced by its interaction with oxygen-containing groups on GO surface[46]. A significant weight loss of ~30% is observed at around 200 °C, which corresponds to the pyrolysis of labile oxygen-containing groups with the generation of CO, CO_2 and water[47]. The sharp loss at around 480 °C is caused by the breakage of sp^2 carbon bonds in the hexagonal structure, thus indicating its thermal decomposition[46].

The nature of the GO surface oxygen-containing groups and the surface properties of the hybrid materials were further investigated by XPS analysis (surveys spectra are reported in Figure S2). Firstly, the gradual increase of zinc content was confirmed by Zn-to-C atomic ratios reported in the Table in inset of Figure S2b. Besides, Figure 3c shows the C 1s core level high resolution spectrum, which is fitted by five components corresponding to carbon atoms in different functional groups. Especially, the C–C sp^3 band appears at 283.75 eV, the C–C sp^2 at 284.55 eV,

the C in C–O, C–OH bonds at 285.85 eV, the carbonyl C=O at 286.55 eV and the carboxylate carbon O=C–O at 288.20 eV[48,49]. Similarly, the O 1s core level high resolution spectrum (Fig. 3d) consists of three components relative to C=O (at 531.20 eV), O–C–O (at 532.10 eV) and C–OH (at 533.15 eV)[50]. The Zn 2p region (Figure 3b) evidences the presence of zinc on the surface of GO, with a signal comparable to that of pure ZnO. The C 1s region (Fig. 3c), instead, shows three components for the hybrid samples, which are ascribable to C–C sp^2, C–O, C–OH and carbonyl C=O bonds. In particular, the last peak is mostly attributed to adventitious CO_2 although some potential contributions, rising from carbonyl groups remaining after the growth of the metal oxide, may not be excluded. The O 1s core level high resolution spectrum (Fig. 3d) have four components centered at around 530.10, 530.60, 531.80 and 533.20 eV. These correspond to lattice oxygen anions (O^{2-}) in the wurtzite structure, to oxygen ions (O^{2-} and O^-) in the oxygen-deficient regions, caused by oxygen vacancies, and to adsorbed oxygen species (especially water molecules)[51]. Interestingly, the content of adsorbed oxygen species is higher for the 4:1 ratio than for both the pure ZnO and the 32:1 ratio, suggesting a more hydrophilic nature of this compound than the others. Hence, from all the above characterizations, it can be concluded that by adopting different zinc salt precursor-to-GO weight ratios, it is possible to gradually cover the surface of graphene oxide sheets creating strong bonds between the graphene and the metal oxide nanoparticles. This gradual growth can influence the surface properties, the morphology and crystal size of the as-prepared powders, thus affecting the final photo- and chemical sensing performances.

View Article Online
DOI: 10.1039/C9NR08901B

Optoelectronic and Chemical Sensing Properties

The optical properties of the zinc oxide-based compounds were initially investigated by UV/Vis absorption spectroscopy. Figure S3a shows the UV/Vis spectra revealing a broad rise in absorption at around 370 nm. To deduce the band gap, both Tauc plot (Fig. S3b) and Kubelka-Munk (Fig. S3c) analyses were pursued, resulting in similar values of 3.00 and 3.10 eV, respectively, which are a little lower than the reported ZnO band gap of 3.37 eV[52]. The synthesized nanopowders were deposited on interdigitated electrodes via a scalable air-spraying method, realizing homogeneous micrometric films (Figures 2d – f). The cross-sectional FESEM images (Fig. 2g – i), reveal a layer thickness of around 2 μm for both ZnO and 32:1 ZnO/GO, the 4:1 ratio results in thicker films of ca ~5 μm (Table 1). The films porosities were also computed indicating values above 90% for all the samples (Table 1). Considering the nanoscale size of the ZnO and GO grains, the micrometer thickness of the ZnO/GO films provide a three-dimensional space for the electron and gas molecules transport. This is supported from the FESEM images of the ZnO/GO films showing a three-dimensional distribution of grains (Figure 2). Previous modeling of the sensing mechanism of similarly three-dimensionally structured films has emphasized that the gas sensing reactions and the electrical transduction mechanisms are best represented by a three-dimensional network of sensing domains[53]. Specifically, Becker *et al.*[54] proposed that the contribution of the grains in the chemical sensing mechanism can be modeled as a three-dimensional network of parallel and series resistances distributed through the film thickness. Moreover, the individual contribution of the various part of the films change significantly as a function of the analyte concentration, sensing temperature and catalytic activity of the grains. As such, the sensing mechanism of the composite films is truly three-dimensional with contributions from the various parts and height of the film.

Hence, Figure 4 shows the chemical sensing responses of the pure ZnO and 32:1 ZnO/GO films towards acetone as a function of the temperature and UV light irradiation. Notably, the irregular shape of the response on 1 ppm may arise from limitations in transient response of the mass flow controllers in the experimental setup, utilized here. In particular, at high temperature (350 °C) without UV light, both pure and hybrid samples can detect acetone in air down to 20 ppb. Specifically, the intensity of the 32:1 ZnO/GO response is around three times higher than the ZnO one (Fig. 4a and b). By decreasing the temperature to 150 °C and RT, it was possible to measure a sensor response towards these low concentrations (from 1 ppm to low-ppb) only with the ZnO/GO composite material and exploiting UV light (Fig. 4c and d), whereas no response was obtained for ZnO in dark conditions and a very high low signal-to-noise ratio was noticed for the other composites (Fig. 5a; and Fig. S7 for a more detailed investigation of the other ZnO/GO ratios). Indeed, with the pristine zinc oxide only relatively high concentrations (8 ppm) of ethanol (as representative analyte) can be detected at RT, showing a fairly low signal intensity as displayed in Figure S4. This may be attributed to the relatively large size of the ZnO grains (77 nm) with respect to the high-performing ones (d_p smaller than 40 nm), reported in the literature[20,33]. Indeed, to the increasing of nanoparticle size corresponds a reduction of the grain boundary density, thus resulting in a resistance to the electron conduction[33]. Moreover, for the hybrid compound, at these lower temperatures, the signal intensity was smaller than at 350 °C, however, a good

View Article Online
DOI: 10.1039/C9NR08901B

signal-to-noise ratio was observed down to 100 ppb. Although an analogous sensor response behavior was also observed for ethanol and ethylbenzene (Fig. S5 and S6), a different level of sensitivity was achieved. Particularly, for all the three detected species (namely ethanol, acetone and ethylbenzene), a distinction between high and low operating temperatures in terms of selectivity can be made. Notwithstanding the very low ppb level towards ethanol and acetone obtained with both ZnO and 32:1 ZnO-GO, the signal intensities by hybrid sample are always definitely higher with respect to those of pure ZnO. Moreover, as concern RT sensing, only with 32:1 ZnO/GO a signal was recorded, even if slightly greater target analytes concentrations were detected. Hence, ethanol resulted in the strongest sensing response followed digressively by acetone end ethylbenzene. Actually, the obtained signal at 1 ppm has an intensity two-times higher with respect to those recorded in presence of acetone or ethylbenzene gaseous molecules. Therefore, it is possible to conclude there is a moderate selectivity degree towards EtOH. This may be attributed to their different chemical structures, *i.e.* presence of polar groups (such as hydroxyl groups) or steric hindrance, thus leading to their different affinity with the zinc oxide surface[55–58]. Indeed, it has been already reported alcohols show higher sensing responses than aldehydes or ketones, and to a greater extent with respect to non-polar/low polar analytes, such as ethylbenzene[57–59]. Notably, selectivity may depend from the metal oxide semiconductor used and ZnO is more selective towards ethanol molecules[60]. The interaction between ethylbenzene molecules and the metal oxide is much more difficult due to the phenyl ring presence leading to lower sensitivity (600 ppb) and lower signal intensity for 32:1 ZnO/GO at RT (Fig. 5a and S6d). Moreover, the intensity signal trend obtained towards the increasing of ethanol and acetone concentration does not resemble a Langmuir-like behavior since no plateau is observable, resulting in agreement with what already reported in the literature[57,58]. Conversely, no oxygen-containing/low-polar compounds, such as ethylbenzene, are already reported to give much lower responses, since oxygen functionalities facilitate the adsorption on the metal oxide surfaces. Hence, its initial trend in Figure 5a may be due to its difficulty in interacting with the ZnO-GO material.

Besides, interestingly, the 4:1 ZnO/GO nanopowders resulted in an irreproducible sensor response (Figure S7a). When the analyte gas molecules were injected into the sensing chamber (at RT with UV light), the current decreased revealing a bad signal recovery. This is probably due to the incomplete GO coverage by ZnO nanoparticles and, hence, the formation of a percolating GO network, which shortcuts the chemoresistive ZnO domains. Indeed, a similar behavior with a rapid decrease in current and no recovery, was also observed with the pure graphene oxide (Fig. S7b), probably due to the many oxygen-containing functional groups, that give rise to stronger chemical interactions with the analyte molecules, hindering the gas desorption. It is, therefore, suggested that the effective sensing material is zinc oxide, while GO helps to detect low VOCs concentrations at RT, under UV light irradiation. Moreover, upon purging of the target analyte molecules, both ZnO and 32:1 ZnO/GO readily recover showing fast response and recovery times (both below 50 s at 350 °C; Fig. 5b and c)[35,61]. Reducing the operating temperature, the response times increases to 80-340 s as a function of the analyzed gas. Interestingly, acetone (Fig. 5b and c, orange triangles) shows the fastest response (80 s) and recovery (90 s) times, also at RT.

In order to explain the synergistic effect between graphene oxide and zinc oxide, characterization of the photocurrent under UV light exposure was carried out. Chen *et al.*[62] have demonstrated the incorporation of low-dimensional carbon material into ZnO nanowires effectively enhances the separation efficiency of photo-generated electron-hole pairs, providing efficient carrier transport pathways. They stated rGO/ZnO-based photodetector has high photoresponsivity ($\sim$16 $A \cdot W^{-1}$), high on/off current ratio (2.81×10^4) and great specific detectivity (1.14×10^{14} Jones), under low UV irradiation (< 10 $\mu W \cdot cm^{-2}$) and at 1.0 V bias. Moreover, uniform and oriented GO/ZnO nanorods have been obtained thanks to the presence of GO that influences the growth process of ZnO nanorods, giving rise to less light scattering and thereby stronger absorption and enhanced photocurrent. Therefore, when the growth time is 1 h, the optimum photocurrent of GO/ZnO nanorods is about 10 times than pure ZnO nanorods, whereas the detectivity reaches 7.17×10^{11} $cm \cdot Hz^{1/2} \cdot W^{-1}$ [63]. Hence, starting from these findings, herein the current response was acquired by applying a bias potential of 1.0 V and by irradiating with UV light at 370 nm (light power density of 19 $\mu W \cdot cm^{-2}$), using both pure and composite ZnO-GO materials (Fig. 6a).

The major figures of merit for photodetectors are the magnitudes of the photo- and dark-currents, responsivity and detectivity (Table 2)[33]. Especially the last parameter quantitatively characterizes the photodetectors performances[33]. Photocurrent values are comparable with data reported in the literature for ZnO[33,62,63] and, among the investigated samples, 32:1 ZnO/GO shows the highest value followed digressively by ZnO and 4:1 ZnO/GO (Table 2, 3rd column). In contrast to the other ZnO-GO composite materials, at a 32:1 ZnO/GO ratio, we observed

that the dark-current is decreased while the photo-current is increased. The drop in dark-current has been attributed in the literature[64–70] to the formation of a heterojunction at the surface of ZnO (n-type) semiconductor and p-type material such as NiO, which decreases the available free carriers. Specifically, Retamal *et al.*[67] stated the occurrence of nanoscale heterojunctions between p-type NiO and n-type ZnO enhances the surface band bending of ZnO nanowires, improving the spatial separation efficiency of photogenerated electrons and holes, thus resulting in a larger number of free electron carriers in the ZnO. This behavior is unlikely to be induced by the presence of more conductive GO domains in the ZnO matrix as the latter would result in an increase of the dark-current, as observed at larger GO ratios of 4:1. Therefore, higher I_{photo}/I_{dark} values of around 1400 for the 32:1 ZnO/GO (Table 2, 4th column) were obtained. Furthermore, the rise and decay times (Table 2, 5th and 6th columns) were comparable to data obtained with highly performing ZnO ultraporous nanoparticle networks[33] and slightly lower for the 32:1 compound. Among the investigated parameters, the responsivity achieved with the 32:1 ZnO/GO ratio is very high at around 33 $A \cdot W^{-1}$ (Table 2 and Fig. 6a) with respect to the literature, while the detectivities (Table 2, 8th column) are comparable to the most performing materials[33,62,63].

This photo-responsivity trend (32:1 ZnO/GO > ZnO > 4:1 ZnO/GO) and the very high figures of merit measured with the 32:1 ratio compound, suggest a potential enhancement mechanism for the chemical and UV light sensing. The proposed mechanism is an extension of that reported by Chen *et al.*[64], who explained the sensing behavior of the n-type semiconductor both under dark and UV conditions[71]. Figure 6e shows a schematic representation of the junction between GO and ZnO with the UV light, under a bias of +1.0 V. In summary, when ZnO is exposed to air, oxygen molecules are adsorbed on its surface withdrawing electrons from the conduction band of the semiconductor, thus forming negatively charged oxygen ions (*i.e.* O_2^-, O^- and O^{2-} depending on the operating temperature[72,73]), which are the effective reactive species. This phenomenon gives rise to a low-conductivity depletion layer at the ZnO surface. However, since the adsorption energy is high[71], the oxygen species are thermally stable and difficult to be removed from the ZnO surface at room temperature, therefore they may not react with VOCs molecules. Hence, no gas sensing response in the dark occurs, as we have confirmed in the current study. To overcome this drawback, herein we coupled the metal oxide with graphene oxide-based material. In particular, GO shows a p-type semiconductor behavior[26–28], especially in presence of a n-type material. Hence, the growth of zinc oxide on its surface can give rise to a p-n junction and as schematically shown in Figure 6e. When the device is irradiated by UV light, the separation of the photo-excited electron-hole couples occurs (Fig. 6e). Specifically, some of these holes can desorb the adsorbed oxygen ions forming O_2 gaseous molecules, thus resulting in either a decrease of the depletion layer width or an increase in the free carrier concentration, *i.e.* a rise in the photocurrent upon UV irradiation[71,74]. Moreover, the higher carrier density can cause more ambient oxygen molecules to adsorb onto ZnO surface, thus creating photo-induced oxygen ions that are less strongly bound and, accordingly, they can react more easily with the VOCs molecules[71]. When the reaction occurs, electrons are released back to the conduction band of the metal oxide, decreasing the ZnO surface depletion layer and, then, increasing the final conductivity. The proposed sensing mechanism was further validated by measurement of the 32:1 ZnO/GO sensor response to NO_2 showing an opposite response direction (resistance increase) with respect to reducing gases, as ethanol, acetone and ethylbenzene (Figure S8). This is in line with the expected charge exchange at the nanomaterial surface, where oxidant species would decrease the concentration of free-carriers in the metal oxide. To provide further evidence of the formation of p-n heterojunctions, we have performed electrochemical characterization of the 32:1 ZnO/GO samples obtained by our synthesis procedures and of composites films of ZnO and GO powders (ZnO+GO), mechanically mixed with the same 32:1 ZnO/GO ratio (Figure 6b). We observed a peculiar and specific behavior of the hybrid 32:1 ZnO/GO with respect to mechanically mixed ZnO+GO. The ZnO+GO composite (Figure 6b, grey line) displays a major contribution of graphene oxide (peak at -0.31 V) and a separated, partially masked, ZnO contribution (peak at -0.33 V). This indicates that in these mechanically mixed samples the GO and the ZnO act as separate electrical domains with no intimate electron/hole exchange. In contrast, the hydrothermally grown 32:1 ZnO/GO samples (Figure 6b, purple line) exhibits a miscellaneous electrochemical behavior between that of ZnO and GO. This indicates an intimate interaction between GO and ZnO, further suggesting the formation of p-n heterojunctions between GO and ZnO. To further confirm the formation of nanoscale heterojunctions, electrochemical impedance measurements were performed in line with previous analysis of similar heterojunctions[75,76]. Figure 6c shows the Bode plots relative to 32:1 ZnO/GO, mechanically mixed ZnO-GO, pristine ZnO, GO and glassy carbon electrode. The EIS data of the glassy carbon/investigated materials/electrolyte interfaces were fitted according to the equivalent

circuits shown in Fig. 6d in line with previous work. A series resistor (R_Ω, ca 15-20 Ω cm^{-2}) was introduced to describe the electrolyte resistance and a R_{DL}/CPE$_{DL}$ parallel circuit was used to model the electrode/electrolyte double layer: R_{DL} is the charge transfer resistance, whereas CPE$_{DL}$ represents a non-ideal double layer capacitance. Moreover, an open Warburg element (R_W) was also added in the fitting circuits to take into account the probe mass transfer process. A constant phase element (CPE) was used instead of a real capacitance, due to the presence of defects and impurities that introduce inhomogeneities in the electrical properties of the investigated materials. The charge transfer resistance (R_{DL}) at the solid-liquid interface (the parameters that changes more when the probe reacts), showed similar values for the 32:1 ZnO/GO (0.05 kΩ cm^{-2}) and GO (0.03 kΩ cm^{-2}), and it is two orders of magnitude smaller with respect to the ZnO one (ca 3.50 Ω cm^{-2}; Table 3), which was in line with the literaure[75–77]. The ZnO+GO, on the contrary, exhibited a behavior close to the ZnO, with a charge transfer resistance of about 1.10 kΩ cm^{-2}. These results show that 32:1 ZnO/GO composite, notwithstanding the almost complete coverage of GO by the zinc oxide nanoparticles, has an efficient charge transfer, and a strongly different behavior than the ZnO. Besides, the CPE$_{DL}$ was very high for the conductive GO material (ca 14 mF cm^{-2} s$^{\alpha-1}$) and quite low for the pure ZnO (ca 1 mF cm^{-2} s$^{\alpha-1}$). Interestingly, the 32:1 ZnO/GO showed an intermediate behavior with a capacitance of ca 5 mF cm^{-2} s$^{\alpha-1}$, which is greater than that of the ZnO+GO one of ca 2 mF cm^{-2} s$^{\alpha-1}$. The EIS technique has been previously used to provide information about the actual presence of a p-n heterojunction, modelling it as a parallel combination of a resistance (R_{HJ}), accounting for the leakage and recombination paths through the p/n-type MOS interface, and a constant phase element (CPE$_{HJ}$), due to the non-ideal capacitance resulting from the depletion region of the p-n junction[75–77]. Notably, 32:1 ZnO/GO plot fitted well this model, while the other investigated materials could be not modelled with the above describe heterojunction circuit. This was particularly evident for the mechanically mixed ZnO-GO. Furthermore, a third circuit (R_1/CPE$_1$, *i.e.* the polarization capacitance) is present representing the interface between the powders and the glassy carbon support. CPE$_1$ values similar or higher than that of the bare glassy carbon indicate the easiness of the polarization processes. This is the case only for the GO and 32:1 ZnO/GO.

Overall, the EIS, CV and photo- to dark-current ratios provide a consistent set of results indicating the formation of a p-n heterojunctions between GO and ZnO domains in the 32:1 ZnO/GO composite.

Conclusions

Here, we have presented the fabrication of a three-dimensional nano-heterojunction network consisting of GO nanodomains well-integrated in a 3D zinc oxide matrix. By varying the GO content, tailored physico-chemical properties were obtained, tuning the final photodetectivity and chemical sensing. Particularly, we observed that high amount of GO hinders the sensor response, due to the formation of interconnected GO domains which short-cut the chemical sensing ZnO regions. In contrast, low GO content results in an optimal n-p type nano-heterojunction architecture with enhanced photodetectivity and chemical sensing properties. These optimal materials achieve a UV light responsivity of about 33 A·W^{-1} and room temperature detection of down to 100 ppb VOC concentrations. Notably, the highest sensitivity and fastest response and recovery times were obtained with the 32:1 ZnO/GO. A distinct sensitivity, and thus selectivity, was observed towards the various VOCs with the strongest response for ethanol, followed by acetone and ethylbenzene. This is possibly attributed to the gas molecules chemical structure and their affinity to the ZnO surface. A mechanism for the enhanced sensing behavior achieved with the optimal 32:1 ZnO/GO nanocomposite structure was suggested based on the formation of a nanostructured network of p(GO) – n(ZnO) junctions. We believe that these findings can pave the way for the development of composite carbon/metal oxide-based devices, for applications extending from optoelectronics to chemical sensing and electrocatalysis.

Conflict of interest

The authors declare no conflict of interest.

Acknowledgements

A.T. gratefully acknowledges the support of the Australian Research Council DP150101939, the Australian Research Council DE160100569 and the Westpac2016 Research Fellowship. All the authors acknowledge the use of the Centre of Advanced Microscopy (CAM) at ANU. G.C. and E.P. acknowledge Prof. Pinuccia Cerrato and Dr. Maria Carmen Valsania, Dipartimento di Chimica and NIS, Inter-department Center, Università di Torino for the TEM image of GO; and Prof. Luigi Falciola and Dott.ssa Valentina Pifferi for the electrochemical measurements.

Supporting Information Description

Figure S1: (a) XRD patterns and (b) FTIR of all the investigated samples. (c, d) Fitted Raman spectra of graphite and graphene oxide. (e) TEM image of pure graphite; Figure S2: XPS surveys of (a) graphite, GO and (b) ZnO-based samples; Figure S3: (a) UV-Vis spectra of both pure and GO-hybrid ZnO films and band gap evaluation by (b) Tauc plot and (c) Kubelka-Munk methods; Figure S4: pure ZnO sensor response (8 ppm of ethanol in simulated air, RT, UV light); Figure S5: (a) pure ZnO and (b–d) hybrid 32:1 ZnO/GO sensors response when exposed to different ethanol concentrations; Figure S6: (a) pure ZnO and (b–d) hybrid 32:1 ZnO/GO sensors response when exposed to different ethylbenzene concentrations; Figure S7: (a) 4:1 ZnO/GO, (b) pure GO, (c,d) 16:1 ZnO/GO sensors responses when exposed to different ethanol concentrations, in simulated air (20% O_2 – 80% N_2) at (a,b,d) room temperature (under UV light) and (c) 350°C. Figure S8: example of 32:1 ZnO/GO response to oxidizing species such as NO_2, at RT by exploiting the UV light.

View Article Online
DOI: 10.1039/C9NR08901B

References

1 S. Gupta Chatterjee, S. Chatterjee, A. K. Ray and A. K. Chakraborty, *Sensors Actuators B Chem.*, 2015, **221**, 1170–1181.
2 U. Latif and F. Dickert, *Sensors*, 2015, **15**, 30504–30524.
3 T. Wang, D. Huang, Z. Yang, S. Xu and G. He, *Nano-Micro Lett.*, 2016, **8**, 95–119.
4 A. Tricoli, N. Nasiri and S. De, *Adv. Funct. Mater.*, 2017, **27**, 1605271.
5 W. Li, X. Wu, N. Han, J. Chen, X. Qian, Y. Deng, W. Tang and Y. Chen, *Sensors Actuators B Chem.*, 2016, **225**, 158–166.
6 V. K. Tomer, S. Devi, R. Malik, S. P. Nehra and S. Duhan, *Sensors Actuators B Chem.*, 2016, **229**, 321–330.
7 J.-H. Kim and S. S. Kim, *ACS Appl. Mater. Interfaces*, 2015, **7**, 17199–17208.
8 D. Chen, Y. J. Yuan and S. Member, 2015, **15**, 6749–6760.
9 Z. Song, Z. Wei, B. Wang, Z. Luo, S. Xu, W. Zhang, H. Yu, M. Li, Z. Huang, J. Zang, F. Yi and H. Liu, , DOI:10.1021/acs.chemmater.5b04850.
10 L. Wang, A. Teleki, S. E. Pratsinis and P. I. Gouma, *Chem. Mater.*, 2008, **20**, 4794–4796.
11 M. Righettoni, A. Tricoli and S. E. Pratsinis, *Chem. Mater.*, 2010, **22**, 3152–3157.
12 A. Naskar, M. Narjinary and S. Kundu, *J. Electron. Mater.*, 2017, **46**, 478–487.
13 K. M. Tripathi, T. Kim, D. Losic and T. T. Tung, *Carbon N. Y.*, 2016, **110**, 97–129.
14 G. J. Zhang, X. X. Guo, S. L. Wang, X. L. Wang, Y. P. Zhou and H. Xu, *J. Chromatogr. B Anal. Technol. Biomed. Life Sci.*, 2014, **969**, 128–131.
15 B. Buszewski, M. Kęsy, T. Ligor and A. Amann, *Biomed. Chromatogr.*, 2007, **21**, 553–566.
16 A. M. K. Janghorban and B. H. G. Neri, *J. Nanoparticle Res.*, 2015, **17**, 1–36.
17 Y. Xu, P. Liu, D. Sun, Y. Sun, G. Zhang and D. Gao, *Mater. Lett.*, 2015, **161**, 495–498.
18 W. Li, S. Ma, Y. Li, G. Yang, Y. Mao, J. Luo, D. Gengzang, X. Xu and S. Yan, *Sensors Actuators B Chem.*, 2015, **211**, 392–402.
19 P. Zhang, G. Pan, B. Zhang, J. Zhen and Y. Sun, *Mater. Res.*, 2014, **17**, 817–822.
20 S.-P. Chang and K.-Y. Chen, *ISRN Nanotechnol.*, 2012, **2012**, 1–5.
21 M. Righettoni, A. Amann and S. E. Pratsinis, *Mater. Today*, 2015, **18**, 163–171.
22 F. Meng, Z. Guo and X. Huang, *Trends Anal. Chem.*, 2015, **68**, 37–47.
23 S. Pei, J. Zhao, J. Du, W. Ren and H. M. Cheng, *Carbon N. Y.*, 2010, **48**, 4466–4474.
24 H. Moussa, E. Girot, K. Mozet, H. Alem, G. Medjahdi and R. Schneider, *Appl. Catal. B Environ.*, 2016, **185**, 11–21.
25 E. Pargoletti, A. Tricoli, V. Pifferi, S. Orsini, M. Longhi, V. Guglielmi, G. Cerrato, L. Falciola, M. Derudi and G. Cappelletti, *Appl. Surf. Sci.*, , DOI:10.1016/j.apsusc.2019.04.046.
26 D. T. Phan and G. S. Chung, *J. Phys. Chem. Solids*, 2013, **74**, 1509–1514.
27 T.-F. Yeh, J. Cihlář, C.-Y. Chang, C. Cheng and H. Teng, *Mater. Today*, 2013, **16**, 78–84.
28 M. Siyar, A. Maqsood and S. B. Khan, *Mater. Sci.*, 2014, **32**, 292–296.
29 B. A. Vessalli, C. A. Zito, T. M. Perfecto, D. P. Volanti and T. Mazon, *J. Alloys Compd.*, 2017, **696**, 996–1003.
30 P. Wang, D. Wang, M. Zhang, Y. Zhu, Y. Xu, X. Ma and X. Wang, *Sensors Actuators B Chem.*, 2016, **230**, 477–484.
31 C. Botas, P. Álvarez, P. Blanco, M. Granda, C. Blanco, R. Santamaría, L. J. Romasanta, R. Verdejo, M. A. López-Manchado and R. Menéndez, *Carbon N. Y.*, 2013, **65**, 156–164.
32 J. Chen, B. Yao, C. Li and G. Shi, *Carbon N. Y.*, 2013, **64**, 225–229.
33 R. Bo, N. Nasiri, H. Chen, D. Caputo, L. Fu and A. Tricoli, *ACS Appl. Mater. Interfaces*, 2017, **9**, 2606–2615.
34 R. Atchudan, T. N. J. I. Edison, S. Perumal, M. Shanmugam and Y. R. Lee, *J. Photochem. Photobiol. A Chem.*, 2017, **337**, 100–111.
35 M. Righettoni, A. Tricoli, S. Gass, A. Schmid, A. Amann and S. E. Pratsinis, *Anal. Chim. Acta*, 2012, **738**, 69–75.
36 C. H. Chen, S. Hu, J. F. Shih, C. Y. Yang, Y. W. Luo, R. H. Jhang, C. M. Chiang and Y. J. Hung, *Sci. Rep.*, , DOI:10.1038/s41598-017-04139-0.

37 T. T. Wu and J. M. Ting, *Surf. Coatings Technol.*, 2013, **231**, 487–491.
38 J. Song, X. Wang and C.-T. Chang, *J. Nanomater.*, 2014, **2014**, 1–6.
39 K. N. Kudin, B. Ozbas, H. C. Schniepp, R. K. Prud'homme, I. A. Aksay and R. Car, *Nano Lett.*, 2008, **8**, 36–41.
40 R. Ramachandran, M. Saranya, P. Kollu, B. P. C. Raghupathy, S. K. Jeong and A. N. Grace, *Electrochim. Acta*, 2015, **178**, 647–657.
41 A. A. Dubale, W.-N. Su, A. G. Tamirat, C.-J. Pan, B. A. Aragaw, H.-M. Chen, C.-H. Chen and B.-J. Hwang, *J. Mater. Chem. A*, 2014, **2**, 18383–18397.
42 E. Pargoletti, S. Mostoni, G. Rassu, V. Pifferi, D. Meroni, L. Falciola, E. Davoli, M. Marelli and G. Cappelletti, *Environ. Sci. Pollut. Res.*, , DOI:10.1007/s11356-017-8430-x.
43 G. Cappelletti, V. Pifferi, S. Mostoni, L. Falciola, C. Di Bari, F. Spadavecchia, D. Meroni, E. Davoli and S. Ardizzone, *Chem. Commun.*, 2015, **51**, 10459–10462.
44 S. Mostoni, V. Pifferi, L. Falciola, D. Meroni, E. Pargoletti, E. Davoli and G. Cappelletti, *J. Photochem. Photobiol. A Chem.*, DOI:10.1016/j.jphotochem.2016.10.003.
45 A. H. Moharram, S. A. Mansour, M. A. Hussein and M. Rashad, *J. Nanomater.*, , DOI:10.1155/2014/716210.
46 E. T. Mombeshora, P. G. Ndungu and V. O. Nyamori, *New Carbon Mater.*, 2017, **32**, 174–187.
47 X. Cai, Q. Zhang, S. Wang, J. Peng, Y. Zhang, H. Ma, J. Li and M. Zhai, *J. Mater. Sci.*, 2014, **49**, 5667–5675.
48 S. Muralikrishna, K. Sureshkumar, T. S. Varley, D. H. Nagaraju and T. Ramakrishnappa, *Anal. Methods*, 2014, **6**, 8698–8705.
49 L. Tang, X. Li, R. Ji, K. S. Teng, G. Tai, J. Ye, C. Wei and S. P. Lau, *J. Mater. Chem.*, 2012, **22**, 5676.
50 M. C. Hsiao, C. C. M. Ma, J. C. Chiang, K. K. Ho, T. Y. Chou, X. Xie, C. H. Tsai, L. H. Chang and C. K. Hsieh, *Nanoscale*, 2013, **5**, 5863–5871.
51 Y. Tu, S. Chen, X. Li, J. Gorbaciova, W. P. Gillin, S. Krause and J. Briscoe, *J. Mater. Chem. C*, 2018, **6**, 1815–1821.
52 N. Nasiri, R. Bo, F. Wang, L. Fu and A. Tricoli, *Adv. Mater.*, 2015, **27**, 4336–4343.
53 A. Tricoli, M. Righettoni and A. Teleki, *Angew. Chemie Int. Ed.*, 2010, **49**, 7632–7659.
54 T. Becker, S. Ahlers, C. Bosch-v.Braunmühl, G. Müller and O. Kiesewetter, *Sensors Actuators, B Chem.*, 2001, **77**, 55–61.
55 R. Zhang, Z. Liu, L. Ling and B. Wang, *Appl. Surf. Sci.*, 2015, **353**, 150–157.
56 M. M. Rahman, S. B. Khan, A. M. Asiri, K. A. Alamry, A. A. P. Khan, A. Khan, M. A. Rub and N. Azum, *Microchim. Acta*, 2013, **180**, 675–685.
57 H. Gong, Y. J. Wang, S. C. Teo and L. Huang, *Sensors Actuators B Chem.*, 1999, **54**, 232–235.
58 B. P. J. de Lacy Costello, R. J. Ewen, N. M. Ratcliffe and P. S. Sivanand, *Sensors Actuators B Chem.*, 2003, **92**, 159–166.
59 R. Rella, J. Spadavecchia, M. G. Manera, S. Capone, A. Taurino, M. Martino, A. P. Caricato and T. Tunno, *Sensors Actuators B Chem.*, 2007, **127**, 426–431.
60 C. P. Gupta, S. K. Sharma, B. Bhowmik, K. T. Sampath, C. Periasamy and S. Sancheti, *J. Electron. Mater.*, 2019, **48**, 3686–3691.
61 M. Righettoni, A. Tricoli and S. E. Pratsinis, *Anal. Chem.*, 2010, **82**, 3581–3587.
62 C. Chen, S. Zhang, B. Hu, H. San, Z. Cheng and W. Hofmann, *Compos. Part B Eng.*, 2019, **164**, 640–647.
63 C. Chen, P. Zhou, N. Wang, Y. Ma and H. San, *Nanomaterials*, 2018, **8**, 26.
64 H. Chen, R. Bo, A. Shrestha, B. Xin, N. Nasiri, J. Zhou, I. Di Bernardo, A. Dodd, M. Saunders, J. Lipton-Duffin, T. White, T. Tsuzuki and A. Tricoli, *Adv. Opt. Mater.*, 2018, **6**, 1800677.
65 N. Nasiri, R. Bo, L. Fu and A. Tricoli, *Nanoscale*, 2017, **9**, 2059–2067.
66 D. Cammi, K. Zimmermann, R. Gorny, A. Vogt, F. Dissinger, A. Gad, N. Markiewcz, A. Waag, J. D. Prades, C. Ronning, S. R. Waldvogel and T. Voss, *J. Phys. Chem. C*, 2018, **122**, 1852–1859.
67 J. R. D. Retamal, C. Y. Chen, D. H. Lien, M. R. S. Huang, C. A. Lin, C. P. Liu and J. H. He, *ACS Photonics*, 2014, **1**, 354–359.
68 J. Li, F. Zhao, L. Zhang, M. Zhang, H. Jiang, S. Li and J. Li, *RSC Adv.*, 2015, **5**, 67610–67616.
69 H. Liu, Q. Zhou, Q. Zhang, C. Hong, L. Xu, L. Jin and W. Chen, *Sensors*, 2017, **17**, 913.
70 T.-F. Yeh, J. Cihlář, C.-Y. Chang, C. Cheng and H. Teng, *Mater. Today*, 2013, **16**, 78–84.

View Article Online DOI: 10.1039/C9NR08901B

71 Z. Q. Zheng, J. D. Yao, B. Wang and G. W. Yang, *Sci. Rep.*, 2015, **5**, 1–8.
72 H. J. Kim and J. H. Lee, *Sensors Actuators, B Chem.*, 2014, **192**, 607–627.
73 H. W. Kim, Y. J. Kwon, A. Mirzaei, S. Y. Kang, M. S. Choi, J. H. Bang and S. S. Kim, *Sensors Actuators, B Chem.*, 2017, **249**, 590–601.
74 M. Z. Film, *Sensors*, 2017, **18**, 50.
75 M. Santamaria, G. Conigliaro, F. Di Franco and F. Di Quarto, *Electrochim. Acta*, 2014, **144**, 315–323.
76 G. Di Liberto, V. Pifferi, L. Lo Presti, M. Ceotto and L. Falciola, *J. Phys. Chem. Lett.*, 2017, **8**, 5372–5377.
77 K. P. Musselman, A. Marin, A. Wisnet, C. Scheu, J. L. MacManus-Driscoll and L. Schmidt-Mende, *Adv. Funct. Mater.*, 2011, **21**, 573–582.

Table 1. Surface area (S_{BET}), total pore volume ($V_{tot.\ pores}$), crystallite domain size by XRD analysis ($<d^{XRD}>$), optical band gap (E_g, by Kubelka-Munk extrapolation) of the synthesized materials. Thickness (by cross-sectional FESEM) and porosity percentage (obtained by means of UV/Vis spectroscopy technique) of the deposited layers.

View Article Online
DOI: 10.1039/C9NR08901B

Sample	S_{BET} ($m^2\ g^{-1}$)	$V_{tot.\ pores}$ ($cm^3\ g^{-1}$)	$<d^{XRD}>$ (nm)	E_g (eV)	Film thickness (μm)	% Film porosity
Graphite	11	0.030	27	–	–	–
GO	30	0.010	11	–	–	–
ZnO	9	0.040	77	3.11	2.1 ± 0.3	93 ± 1
4:1 ZnO/GO	25	0.080	22	3.13	5.0 ± 0.6	97.4 ± 0.3
32:1 ZnO/GO	11	0.050	40	3.07	2.0 ± 0.1	92.8 ± 0.4

Table 2. Figures of merit of photodetectors made by Zn-based samples (λ = 370 nm, light power density = 19 μW cm^{-2}, applied bias = +1.0 V).

View Article Online
DOI: 10.1039/C9NR08901B

Sample	Dark-current (μA)	Photocurrent (μA)	I_{Photo}/I_{Dark}	Rise time (s)	Decay time (s)	Responsivity ($A \cdot W^{-1}$)	Detectivity (Jones)
ZnO	1.08	39	37	≈160	≈190	5.2	5.5×10^{12}
4:1 ZnO/GO	0.01	≈2	167	≈150	≈160	≈0.3	2.6×10^{12}
32:1 ZnO/GO	0.18	257	1426	≈100	≈120	33.4	8.7×10^{12}

Table 3. EIS fitting parameters according to the computed equivalent circuits, at -0.15 V. Supporting electrolyte: PBS 0.1 M, pH 7.4. Adopted probe: $[Ru(NH_3)_6]Cl_3$, 3 mM.

View Article Online
DOI: 10.1039/C9NR08901B

Modified-GCE	R_Ω (Ω cm^2)	R_{ct} (kΩ cm^2)	CPE_{DL} (mF cm^{-2} s$^{\alpha-1}$)	R_{HJ} (Ω cm^2)	CPE_{HJ} (mF cm^{-2} s$^{\alpha-1}$)	R_1 (kΩ cm^2)	CPE_1 (mF cm^{-2} s$^{\alpha-1}$)	R_W (Ω cm^2)
Bare	21.90	2.95	1.41	–	–	1.96	1.98	–
GO	15.73	0.03	13.70	–	–	4.50	2.01	0.02
ZnO	19.27	3.48	1.05	–	–	11.20	0.83	–
32:1 ZnO/GO	17.47	0.05	4.84	1.40	0.30	5.57	1.60	3.07
ZnO+GO	17.81	1.10	2.15	–	–	7.59	0.62	3.23

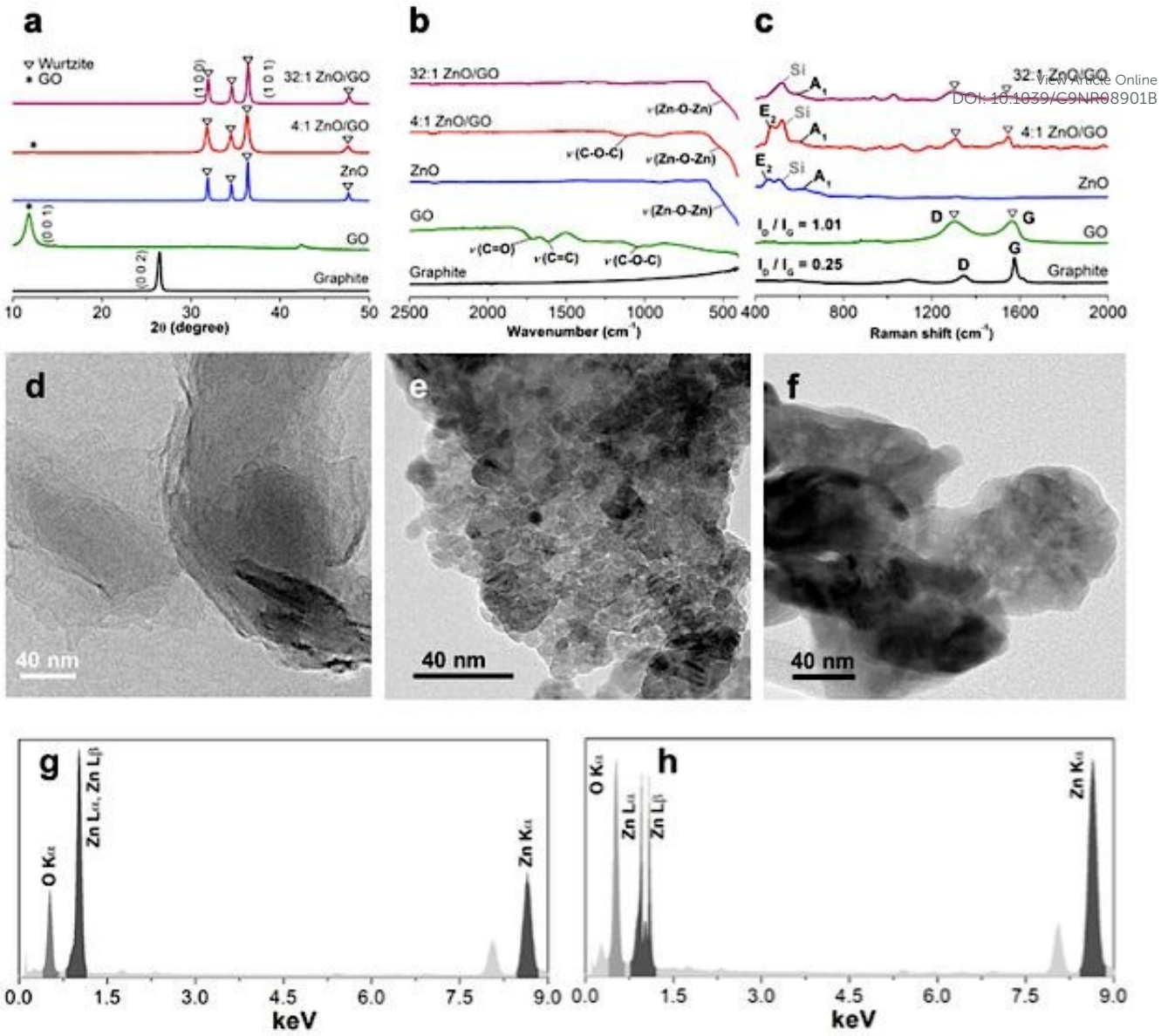

Figure 1. (a) XRD patterns of graphite, graphene oxide (GO), pure ZnO and hybrid ZnO/GO nanocomposites (100% intensity reflection planes have been assigned to the main phase of each compound). (b) FTIR and (c) Raman spectra (in the case of ZnO-based compounds, Si Raman band[59] due to the adopted support has been highlighted in grey color) of all the investigated samples. TEM images of (d) GO, (e) 4:1 ZnO/GO and (f) 32:1 ZnO/GO. EDX spectra of (g) 4:1 ZnO/GO and (h) 32:1 ZnO/GO samples.

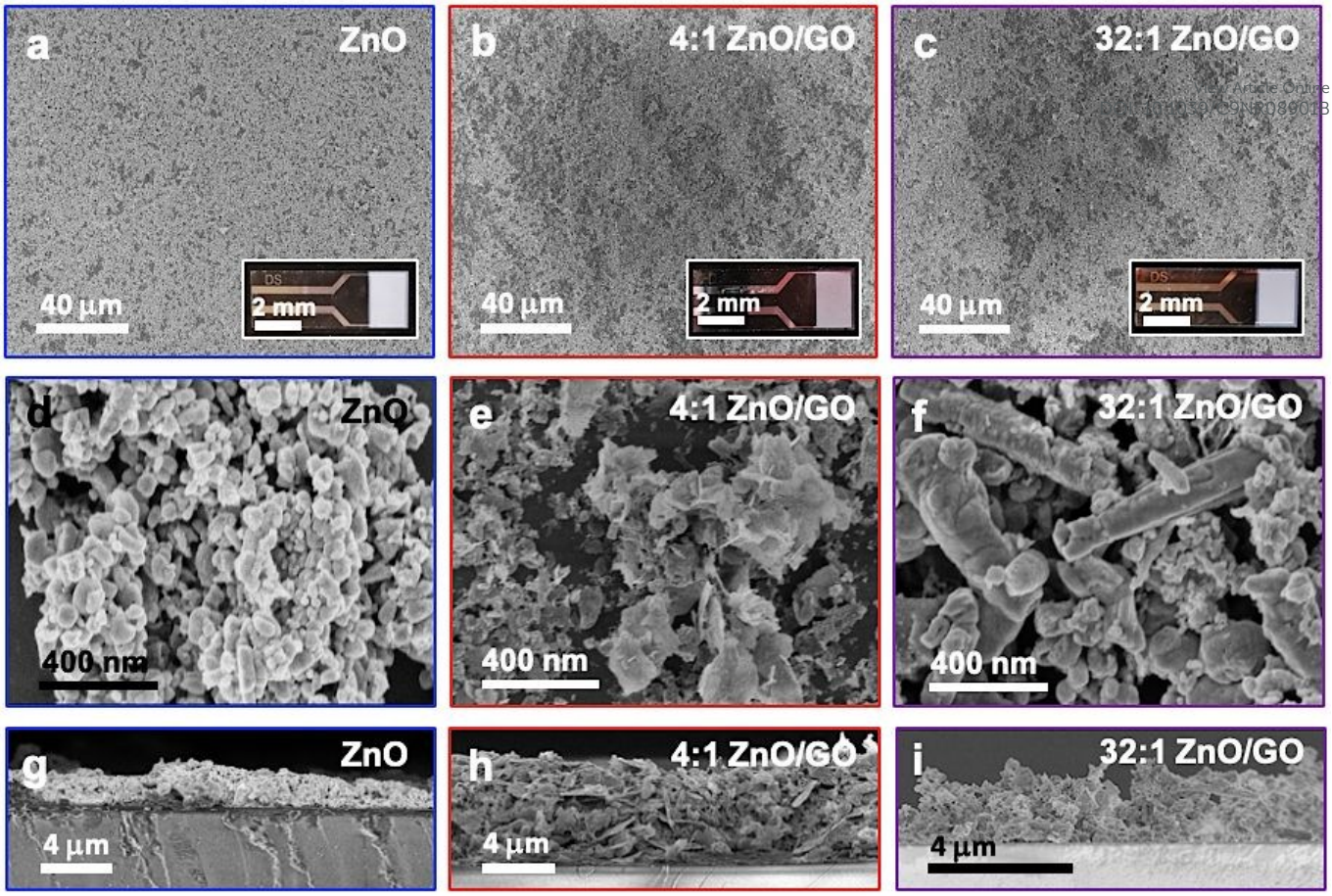

Figure 2. FESEM images of either pure ZnO or hybrid ZnO/GO samples. (a–f) Top view and (g–i) cross-sectional images. Insets: photos of the relative interdigitated electrodes.

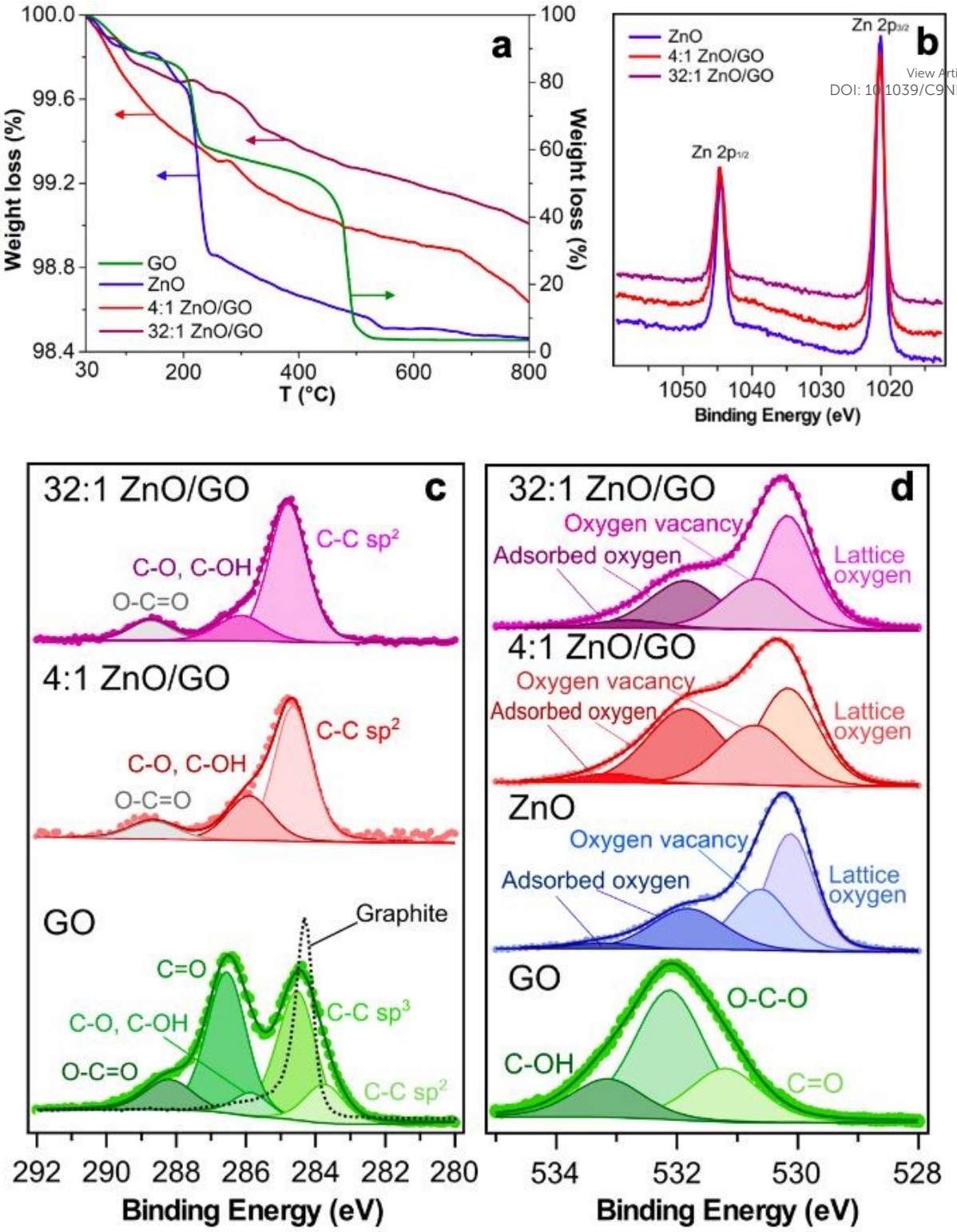

Figure 3. (a) TGA spectra of GO, pure and hybrid nanopowders. XP spectra of (b) Zn 2p region of ZnO, 4:1 ZnO/GO and 32:1 ZnO/GO; (c) C 1s and (d) O 1s regions of GO (graphite, black dotted line) and hybrid samples.

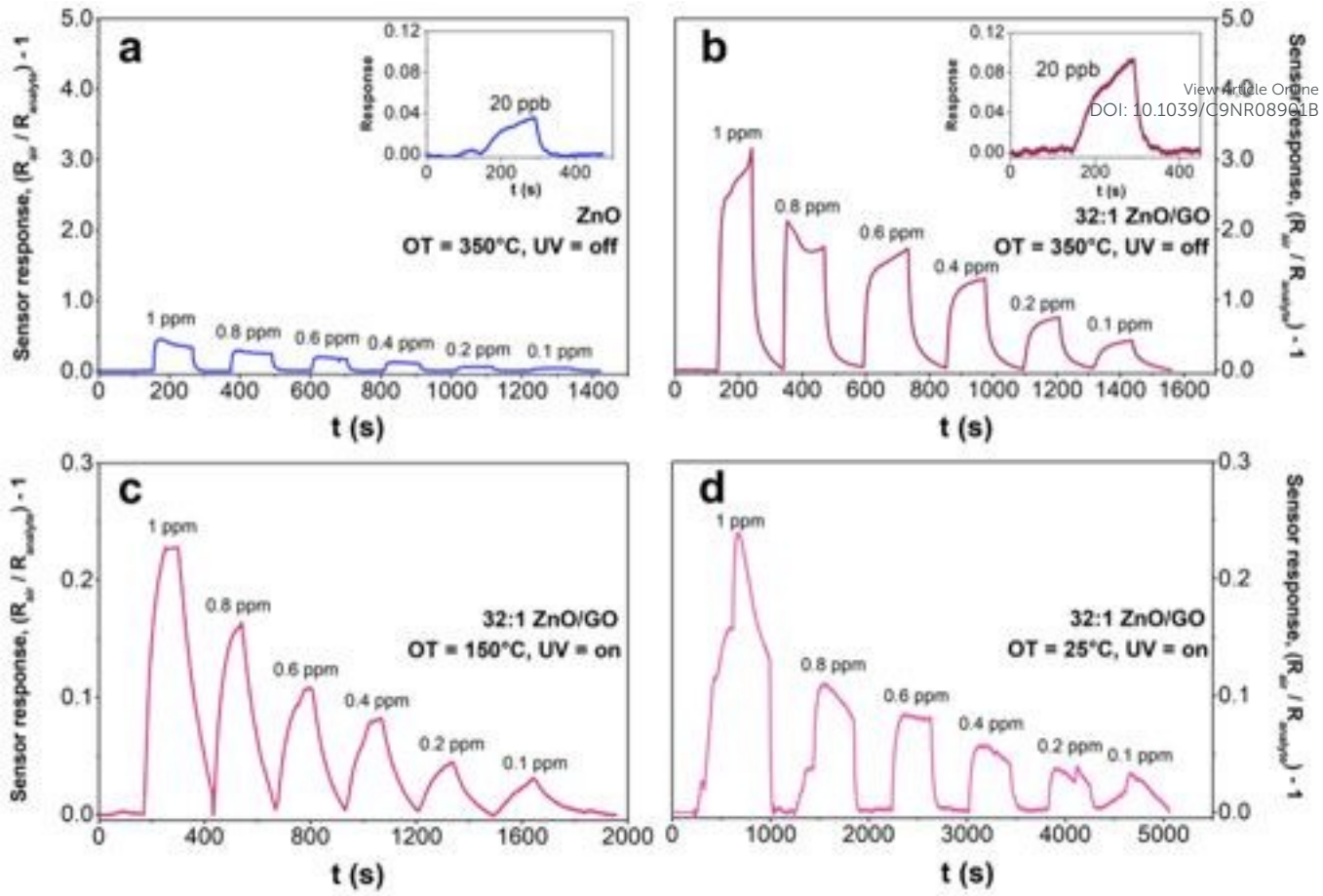

Figure 4. (a) Pure ZnO and (b–d) hybrid 32:1 ZnO/GO sensors response when exposed to different acetone concentrations (1 ppm to 20 ppb) in simulated air (20% O_2 – 80% N_2). OT = Operating Temperature.

View Article Online
DOI: 10.1039/C9NR08901B

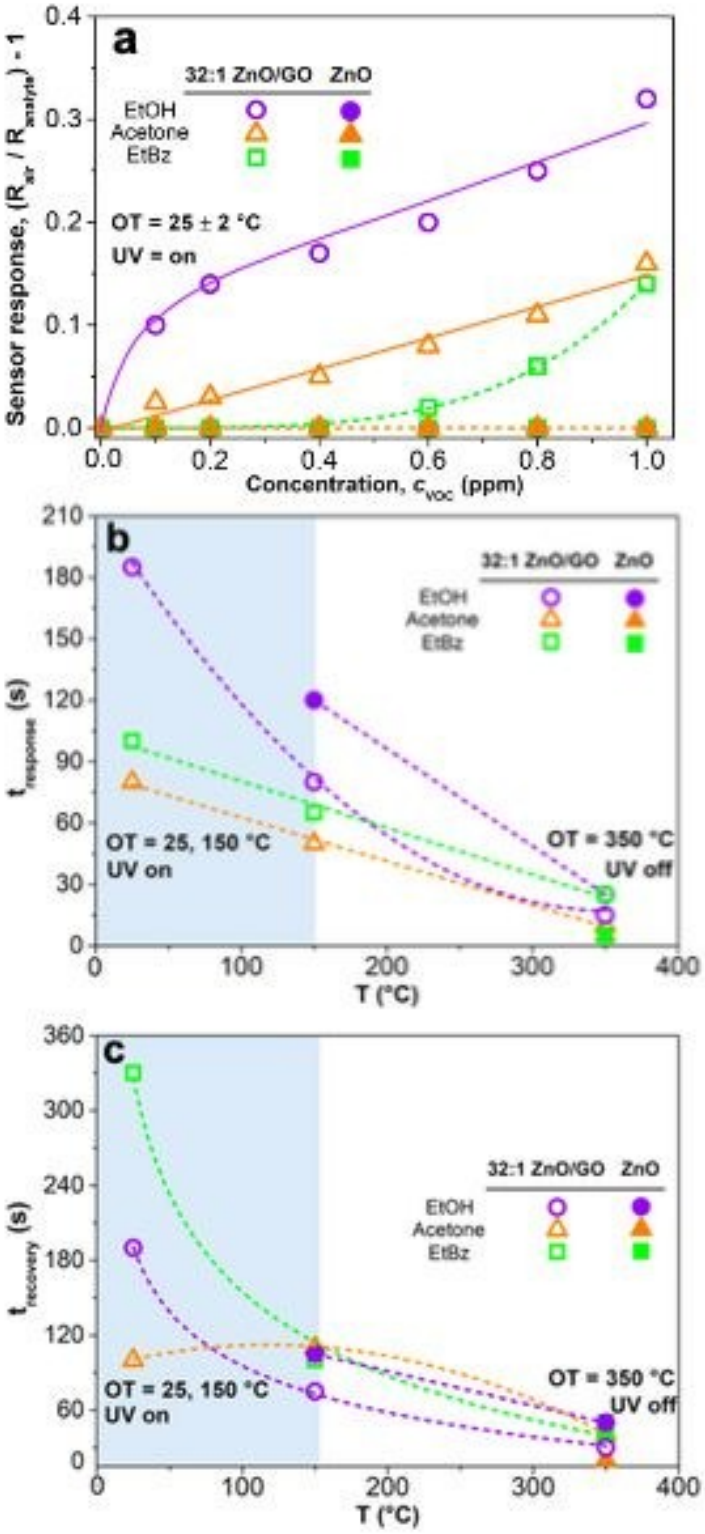

Figure 5. (a) Signal response versus different VOCs concentrations obtained with either 32:1 ZnO/GO or pure ZnO. (b) Response and (c) recovery times as a function of the Operating Temperature (OT).

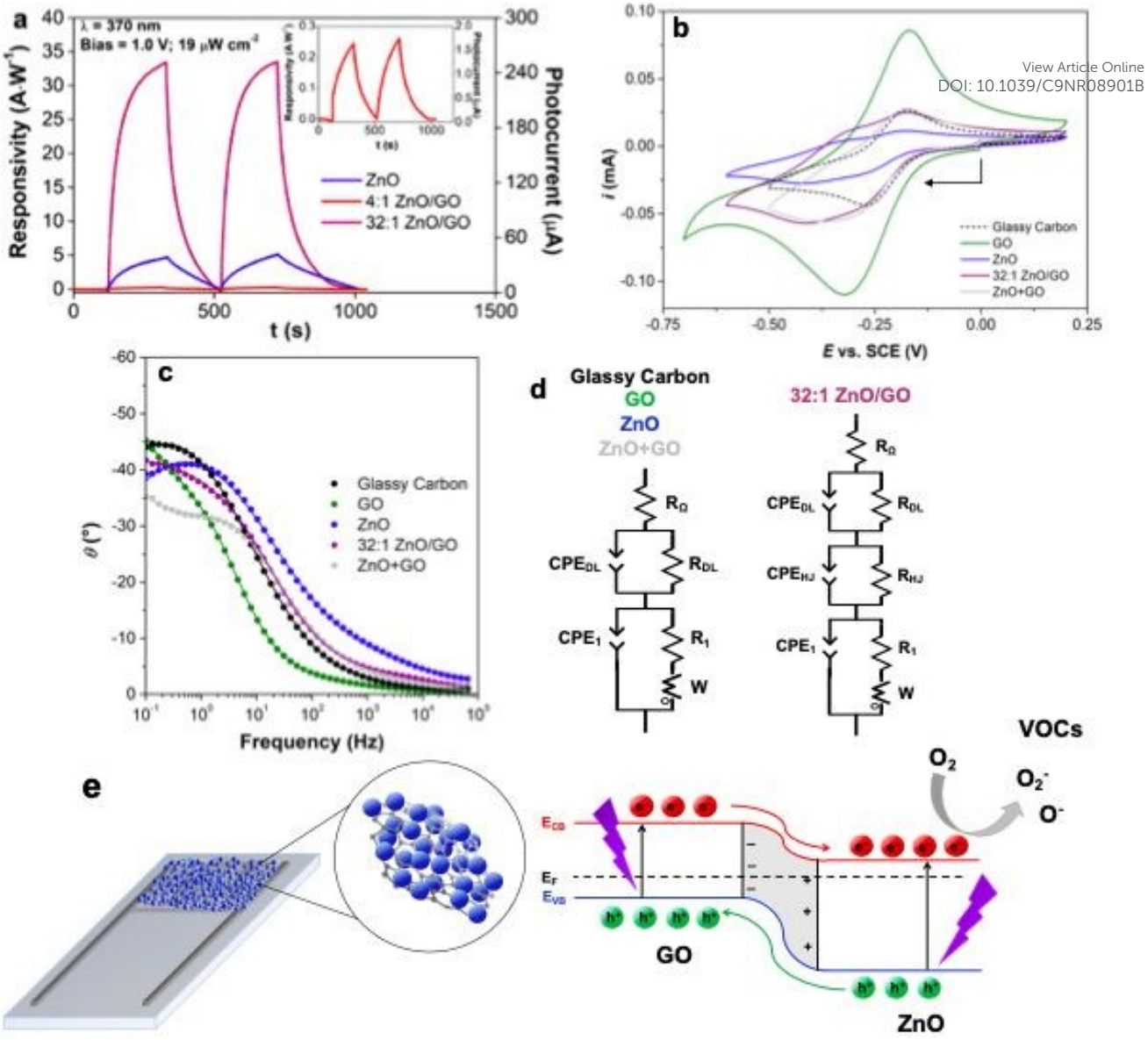

Figure 6. (a) Dynamics of responsivity and photocurrent for all the Zn-based samples (λ = 370 nm, light power density = 19 μW cm^{-2}, applied bias = +1.0 V). (b) Cyclic voltammograms relative to both bare and modified glassy carbon electrodes, in the presence of 3 mM $[Ru(NH_3)_6]Cl_3$ probe (electrolyte 0.1 M PBS, scan rate: 100 mV s^{-1}). (c) Impedance Bode plots recorded for glassy carbon, GO, pure ZnO, 32:1 ZnO/GO and mechanically mixed ZnO+GO, recorded in 0.1 M PBS at -0.15 V (potential at which the adopted probe, $[Ru(NH_3)_6]Cl_3$, is oxidized). Points are the experimental values, while continuous lines are the simulated data according to the equivalent circuits, shown in (d). (e) Schematic model of GO-ZnO p-n junction for hybrid materials under UV and with +1.0 V applied bias (E_{VB}, E_{CB}, E_F are energies of Valence Band, Conduction Band and Fermi level).

View Article Online
DOI: 10.1039/C9NR08901B